SharpViSu: integrated analysis and segmentation of super-resolution microscopy data

Supplementary Material

Leonid Andronov[1,2,3,4], Yves Lutz[1,2,3,4], Jean-Luc Vonesch[1,2,3,4] and Bruno P. Klaholz[1,2,3,4,*]

[1]Centre for Integrative Biology (CBI), Department of Integrated Structural Biology, IGBMC (Institute of Genetics and of Molecular and Cellular Biology), 1 rue Laurent Fries, Illkirch, France, [2]Centre National de la Recherche Scientifique (CNRS) UMR 7104, Illkirch, France, [3]Institut National de la Santé et de la Recherche Médicale (INSERM) U964, Illkirch, France and [4]Université de Strasbourg, Strasbourg, France.

*To whom correspondence should be addressed.

Supplementary Results and Discussion

To evaluate the precision of the drift correction in SharpViSu, we modulated data by adding a perfect circular-shape drift with a radius of 25 nm to a corrected dataset acquired with a β-tubulin-labelled sample. The direction and the amount of the drift obtained by cross-correlation is very similar to the introduced drift (Supplementary Fig. S1A). The algorithm was able to retrieve the original data with high accuracy: the resolution of the distorted dataset after 5 iterations of drift correction improved from 75.5 ± 1.1 nm to 50.2 ± 0.7 nm which equals to the initial resolution within the statistical error (Supplementary Fig. S1B).

Drift can be difficult to correct in the case of structure-less data. In the limit of randomly distributed localizations, cross-correlation peaks are located in random positions, leading to wrong values of the offset. Therefore, a redundancy in the experimental data is required for correction of drift by cross-correlations. Otherwise, fiducial markers should be introduced into the sample. The drift correction with fiducials by means of SharpViSu consists in choosing a small region of interest with the image of a bead, cross-correlation calculation of the drift from this small region, and application of the drift correction to the original dataset.

It should be noted that drift produces a shift between multi-color images in the case of sequential acquisitions. While the chromatic aberrations of the objective can be considered constant over time, drift is obviously variable. That is why simultaneous correction of both chromatic aberration and drift is indispensable for any multi-color experiment.

To demonstrate the ability of the software to correct data with chromatic aberrations we precalibrated our microscope using localization datasets with TetraSpeck multi-color beads (200 nm in diameter). After merging all the events within a radius of 100 nm and eliminating those with less than 10^5 photons, we obtained 26 events in each of the three channels, each event corresponding to the center of the point spread function (PSF) of a given bead (Supplementary Fig. S2A). The distances between the doublets of localizations were fitted with a 2-order polynomial function (Supplementary Fig. S2B). The second order of the polynomial was chosen, after testing, because it did not produce any edge effects. The quality of the fit is readily evaluable from our software.

To assess the precision of the fit and performance of double-color drift correction we simulated a typical super-resolution experiment by acquiring images of the beads first through the 642 nm channel and then through the 488 nm channel. The raw data from the microscope demonstrated significant chromatic aberrations and drift, in total up to 70 nm of distance between the images of each bead in the two colors (Supplementary Fig. S2C). This value is much worse than the localization precision, and would obviously lead to a significant loss in resolution and to misinterpretation of results. After correction for drift and chromaticity, the offset between channels dropped to less than 20 nm for the whole field of view, a value acceptable for super-resolution microscopy (Supplementary Fig. S2D).

Multiple localizations of the same fluorophore can affect quantification of super-resolution experiments. This happens if the on-time of the fluorophore is greater than the exposure time of the acquisition frame, or if the boundary between two frames occurred during the shining of the dye, or if the fluorophore came to the "on-state" more than once during the time of acquisition. In the first two cases, the image of the dye appears on a few consecutive frames in the approximately same position. Signals from these localizations can be effectively merged into a single event, averaging the coordinates of the original events and summing the photon counts. The obtained localization has therefore higher precision.

We applied the described filtration to a drift-corrected β-tubulin dataset. As a result, the mean and the median values of the distribution of the number of photons collected in the event increased from 673 and 573 to 1428 and 889 respectively (Supplementary Fig. S3). This means that the average precision of localization improved 1.46 times. In other terms, before correction half of the localizations was determined with a precision better than 24 nm, after filtration this value improved to 19 nm. Precision here means the full width at half maximum of the corresponding Gaussian distribution with the standard deviation determined by formula (1, see the methods section). The less-precise localizations can be further rejected by means of the software imposing a minimum limit on the required photon counts. The regions with too high dye concentration that have not gone completely into the dark state appear on many consecutive frames and merge to a localization with a very high intensity. Such events can be rejected by introducing an upper limit on the photon count. In the above example, we only kept localizations with less than 10^4 photons (Supplementary Fig. S3B).

There are several methods to obtain the 3D coordinates of a fluorophore, including astigmatism (Huang *et al.*, 2008) bi-plane detection (Juette *et al.*, 2008) and double-helix PSF (Pavani *et al.*, 2009). SharpViSu provides a way to calibrate the astigmatic deformation of the PSF for the determination of the Z-position of dyes. The whole calibration process relies on localization tables with fitted positions and sizes (σ_x, σ_y or equivalent values) of the PSF for different Z-distances. The calibration should be done for every color channel that is intended for 3D imaging because of chromatic aberrations of the cylindrical lens and the objective. We provide two possibilities for multi-color calibration of the astigmatism. First, the imaging of multi-color beads should be done for all colors with the very same Z-positions. The obtained calibration curves $\Delta\sigma = \sigma_x - \sigma_y = f(z)$ can be readily applied to experimental data. Second, one can acquire calibration data for each color separately, keeping only the step in Z-positions of the objective constant. In order to consider the axial chromatic aberration, the offset in Z at the point where the PSF is closest to symmetrical should be measured separately and provided to the software. Alternatively, the offset in $\Delta\sigma$ near the $\Delta\sigma = 0$ in the same Z-position for all colors can be used (Supplementary Fig. S4).

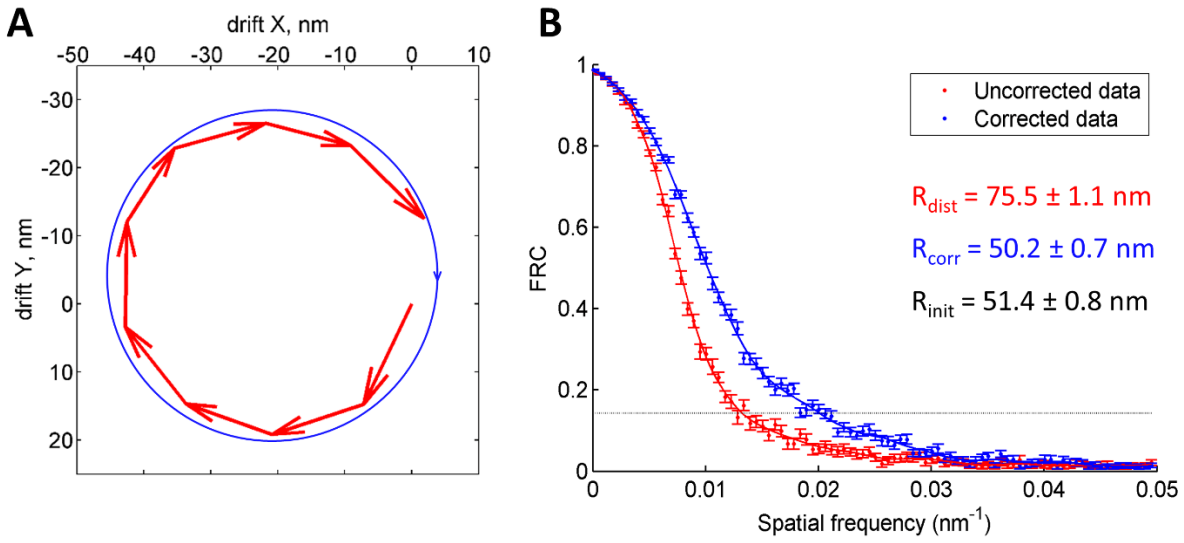

Supplementary Figure S1. Evaluation of drift correction with simulated circular-shape drift. (**A**) Red arrows show drift calculated by our algorithm from the data with artificial circular-shape drift. The blue circle with a radius of 25 nm shows the shape of the simulated ideal circular drift. (**B**) FRCs of the distorted data (red) and the corrected data (blue) show considerable improvement in resolution, with the resolution of the corrected data (R_{corr}) approaching the resolution of the initial non-distorted dataset (R_{init}); R_{dist}, the resolution of the artificially drifted dataset.

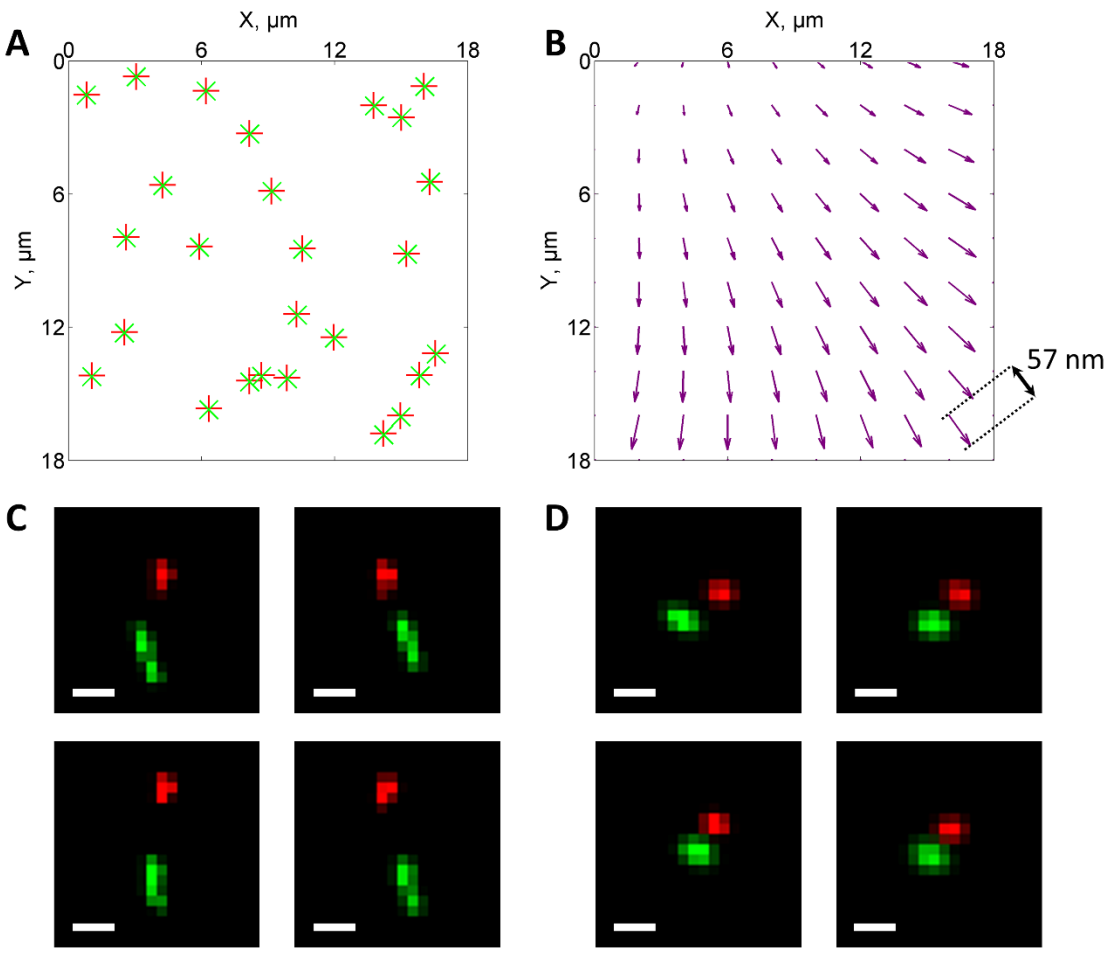

Supplementary Figure S2. Double-color correction of drift and chromatic aberrations. (**A**) Centers of images of 26 multi-color beads, detected with our algorithm. (**B**) Fit of the field of view of the objective with a second-degree polynomial. The arrows indicate the offset between the red and the green channels, multiplied 30 times for visualization. (**C-D**) Multi-color experiment simulated with Tetraspeck fluorescent beads. Each image shows a pair of images of a single bead, acquired through different color channels. The four images correspond to beads found in the corresponding corners of a single field of view. (**C**) Raw data demonstrate an offset due to chromatic aberrations and drift. (**D**) The same beads after correction of the chromatic aberrations using the fit (**B**) and the sequential drift correction. Red and green: imaging with excitation of 642-nm and 488-nm lasers accordingly. The images are in histogram representation with a pixel size of 5 nm. Scale bars: 20 nm.

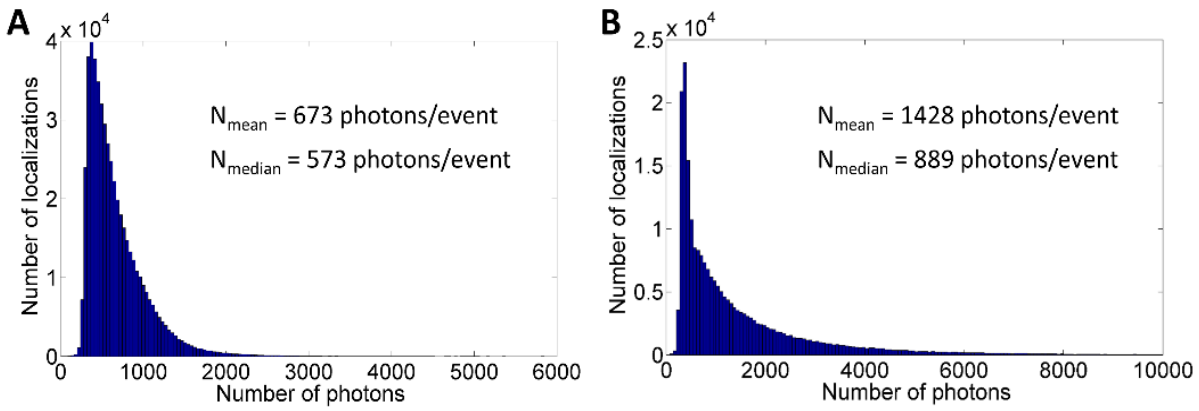

Supplementary Figure S3. Sieving of datasets. (**A**) Histogram of the distribution of the number of photons per localization calculated from the raw data. (**B**) The histogram after merging consecutive events within a radius of 50 nm and subsequent removing of localizations with more than 10^4 photons demonstrates increased mean (N_{mean}) and median (N_{median}) photon counts, illustrating the improvement of the localization precision.

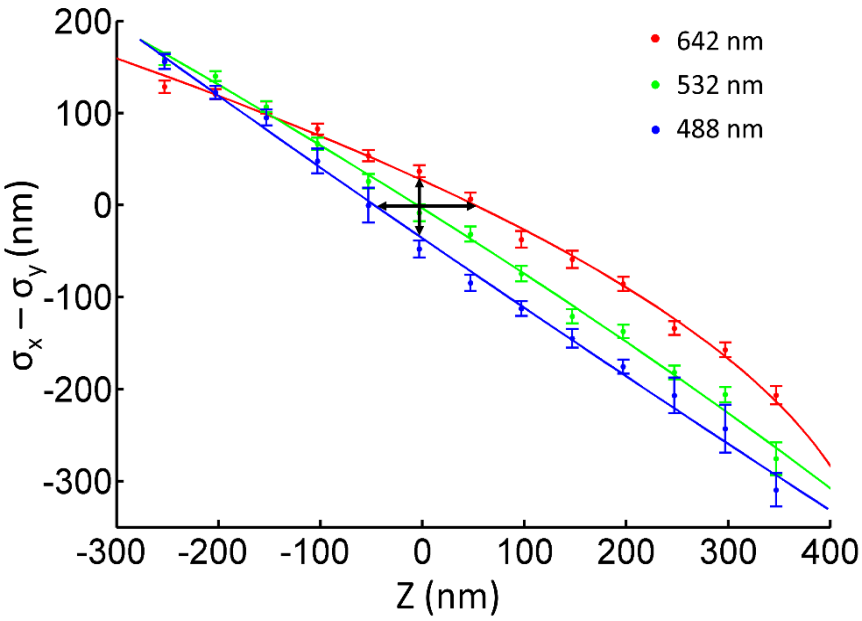

Supplementary Figure S4. Calibration of astigmatism by means of SharpViSu. The experimental points show mean values of $\Delta\sigma = (\sigma_x - \sigma_y)$ of a dataset, acquired at corresponding Z-positions of the objective with multi-color beads as sample. The error bars indicate standard deviations of the distribution of $\Delta\sigma$ for each position. The curves represent 2-order polynomial fits of the distributions. The horizontal arrow at $\Delta\sigma = 0$ nm indicates axial chromatic aberration of the system between the corresponding wavelengths. The vertical arrow at Z = 0 nm indicates the difference between $\Delta\sigma$ of the PSF of the corresponding color channels. These arrows represent the parameters that can be optionally used for calibration in SharpViSu.

	Sharp ViSu	PALM siever	ViSP	Quick PALM	Rapid STORM	LM µManager	Rain STORM	Thunder STORM
Platform	Matlab, stand-alone	Matlab	Stand-alone	ImageJ	Stand-alone	ImageJ	Matlab, stand-alone	ImageJ
Multi-channel	+	-	++	-	++	+	++	-
Drift correction	++	++	-	+	+	+	+	++
Chromatic correction	++	-	+	-	++	++	++	-
Fourier ring correlation	+	+	-	-	-	-	-	-
3D determination	+	-	-	+	+	+	-	+
3D viewer	+	+	++	-	-	-	-	+
Grouping of localizations	+	+	-	-	-	+	-	+
Local density visualization	+	+	+	-	+	-	-	+
Cluster analysis	++	+	+	-	+	-	-	-
Fitting of raw images	-	-	-	+	+	+	+	+

Supplementary Table S1. Comparison of SharpViSu with other open-source software for processing of localization microscopy data. Drift correction: "+", drift correction with fiducial markers; "++", also drift correction without fiducials. Chromatic correction: "+", only translation and scaling with manual parameters; "++", calibration with flexible transformation. 3D viewer: "+", slice viewer; "++", 3D volume viewer. Multi-channel: "+", 2 channels; "++", 3 or more channels. Grouping of localizations: averaging localizations within a given radius in consecutive frames. Cluster analysis: "++", comprehensive analysis including Ripley and Voronoi analysis with Monte-Carlo simulations and statistics on properties of detected cluster; "+", one of clustering methods available (either Ripley's K function, DBSCAN, or segmentation based on local density).

Process		**Time**
Loading dataset: 46 MB ASCII file exported from the Leica SR GSD software		1.5 s
Cross-correlation drift estimation and correction: histogram image (20 nm/pix), 11 subsets		6 s / iteration
Grouping consecutive events: R = 50 nm, ≤ 1 empty frame		15 s
FRC: histogram image (10 nm/pixel), 90 frequency points		5.5 s
Visualization	Histogram: 10 nm/pixel	0.5 s
	Gaussian: 10 nm/pixel	35 s
	Voronoi density: 10 nm/pixel	23 s
	Adaptive histogram: max bin capacity = 5	6 s

Supplementary Table S2. Computational time for some data processing steps in SharpViSu (stand-alone application) on example of a tubulin-labelled dataset with around $5 \cdot 10^5$ localizations. PC: i7-4770, 32GB RAM, Win7 x64.

Methods

Software

The software is written in Matlab 8.3 (The MathWorks Inc., 1984-2014). The GUI is built using GUIDE (The Matlab GUI Layout Editor). The software is designed to work with one or two sequentially or simultaneously imaged eventlists, called "red" (the firstly imaged channel) and "green" (the secondly imaged one, if present) for convenience. Besides that, for the "green" eventlist there is a possibility of choosing from two different imaging channels, e.g. for excitation laser lines 488 nm and 532 nm.

SharpViSu supports localization tables from Leica LAS AF, QuickPALM (Henriques *et al*., 2010), RapidSTORM (Wolter *et al*., 2012) or Localization Microscopy plugin for Micro-Manager (Edelstein *et al*., 2014).

For calibration of the objective for chromatic aberrations, one can use raw localization tables corresponding to super-resolution acquisitions of multi-color beads. To get the average positions of the centers of the beads throughout the frame, the events in consecutive frames are merged within a specified radius. Individual spread events are omitted by a threshold on the number of photons, controlled by a histogram. Finally, for the calibration only pairs of events located within a specified radius are taken into account. If there is more than one neighbor within the radius, this pair is excluded from the fit. The shift between the points is fitted with a 2D polynomial of a selectable degree (2-4, default 2) using Matlab's 'fitgeotrans' function. The obtained transformation objects are saved in the installation directory as files '488.mat' and '532.mat' describing the transformation of coordinates of the corresponding channels relative to the red one. The fit can be shown as a vector field on a regular grid. It is possible to load transformation objects from different fits to estimate the correction for the current experiment. During the correction, the transformation is applied to the 'green' eventlist with the Matlab function 'transformPointsInverse'. Optionally, it is possible to use predefined pairs of coordinates that are supposed to coincide on the corrected image.

Drift is calculated as follows: the entire eventlist is divided into n consecutive blocks with equal number of events in each of them (Szymborska, *et al*., 2013). From each of the blocks a histogram image is built for a 20 nm pixel size (by default, as the fastest and a robust enough method in our hands; the Gaussian and Voronoi representations are available with different sampling). Translation between each pair of consecutive images is calculated with subpixel precision by cross-

correlation using ‘dftregistration’ function (Guizar-Sicairos, *et al*., 2008). The (n-1) values of the offset are stored and used for graphical representation with vectors in the corresponding windows with ‘quiver’ function on an ‘axes’ graphics object. For representation, the values of the first and the last offset are multiplied by 1.5 to better account for the full acquisition range. For the correction of the calculated drift, the initial eventlist is divided into (n-1) sublists with borders on the centres of the n blocks used for the calculation of the drift. The first sublist contains the events from the beginning to the centre of the second block; the last sublist contains the events from the centre of the (n-1)th block until the end of the eventlist. The value of the total drift (including the drift in the preceding sublists and the drift from the beginning of the current sublist) is subtracted from the coordinates of each event. In the case of sequential two-color acquisition, the drift value for the events of the firstly imaged channel is calculated as the sum of drift in all the following frames and this value is added to the coordinates of the event in order to bring the drifted localizations towards the final frame of the channel. This procedure eliminates the additional shift between two sequentially imaged channels due to drift.

To merge consecutive events for a given localization the code checks whether there is an event in the following frame within a given Euclidean distance (default 50 nm). If so, it remembers the parameters of the consecutive event for comparison with the next frame. The procedure is iterated until there is no event in the next following frame. Then, the coordinates and standard deviations of all the retrieved events are averaged and the photon counts are added. The obtained average localization replaces the localization on the first frame in the series; the rest of the consecutive events are removed from the eventlist. If the number of “empty” frames is greater than zero, the procedure continues until there are no more than specified number of empty consecutive frames within the radius.

The histogram image representation is built with the ‘hist3’ function with edges generated for the specified pixel size. Quad-tree visualization image (Baddeley *et al*., 2010) is assembled from several histogram images with different pixel sizes, decreasing with a two-times step from half-size of the field of view until such a small size that no pixels have values greater than the required bin capacity. Then, all the images are resized to the maximal size, the excess overlapping regions are removed, and the final image is created by calculating the sum of the histogram images. The brightness of each cell in the final image is proportional to the number of events detected within its region, divided by the cell’s area.

The idea of Gaussian representation is to render the localization precision. It is achieved by displaying each event as a Gaussian kernel centered on (x, y) coordinates of the localization, with the standard deviation

$$\sigma = A/\sqrt{N} \tag{1}$$

where N – number of photons detected in the event; $A = \sigma_{psf} = 0.21 \cdot \lambda / NA$, σ_{psf} – standard deviation of the PSF of the microscope, λ – wavelength of detection, NA – numerical aperture of the objective (Abbe, 1873; Born & Wolf, 1999). The formula (1) approximates the localization precision as function of the number of detected photons (Thompson, *et al.*, 2002; Ober *et al.*, 2004). However, the real value of the localization precision depends on the accuracy of the localization software, calibration of the camera, type of noise, emitter properties etc. (Rieger & Stallinga, 2014; Deschout *et al.*, 2014; Endesfelder & Heilemann, 2014). We determined experimentally $A \approx 240$ nm on our system by measuring the spread of the distribution of localizations of a single object (fluorescent bead) for different N and λ. This gives sufficiently precise estimation of the localization precision for display purposes.

As opposed to Delaunay triangulation (Delauney, 1934), the Voronoi diagram has the advantage that each data point is situated inside an individual cell (Voronoi, 1908), so it is possible to use the value of the inverse area of the cell as the local density in the neighborhood of the data point. The Voronoi diagram is built using Matlab's function 'voronoin'. The values of the local densities are interpolated to a regular grid with selectable cell size using Natural Neighbor interpolation (Sibson, 1981; Matlab's function 'griddata' with option 'natural') which was the best option among those available in Matlab in terms of speed and precision. The interpolation avoids the usage of smoothening methods that are indispensable to get an interpretable image from a directly triangulated image plane (Baddeley *et al.*, 2010). The grid is then transformed onto the image using the points of the grid as the centers of the corresponding pixels. To avoid edge effects during interpolation, the initial points lying near the borders of the field of view that have undefined Voronoi cells are considered to have zero density. If some points have exactly the same coordinates, only one point from this set is kept for the Voronoi triangulation, and the local density at this point is multiplied by the number of experimental points in the spot.

For the "time in color" representation, the image is firstly formed in hue-saturation-value (HSV) color space (Smith, 1978) with H values representing the time where H = 0° (red) corresponds to

the first frame and H = 240° (blue) corresponds to the last one, and V values representing the relative number of events in the pixel; the S value is always set to 1. The V values are multiplied by a specified multiplier to increase contrast.

To select a region of interest (ROI), a binary mask associated with a super-resolution image (histogram representation, pixelation chosen by user) is built interactively with the 'roipoly' function of Matlab. The software then checks in which pixel each event is situated; depending on the mask value in this pixel and selected option (Keep or Clear ROI), the event is either kept or removed from the eventlist.

The calculation of the Z-coordinate of events is based on the difference between standard deviations of Gaussian-shape spots of individual molecules in x and y directions that appears in the case of astigmatism. The fitted values of σ for each event should be present in the dataset. The astigmatism is calibrated as $f(z) = \sigma_x - \sigma_y$, fitted with a polynomial (2nd degree by default) (Henriques *et al*., 2010) using Matlab's 'polyfit'. The fit is used for determination of the Z-position of the fluorophore. The effect of the refractive index of the imaging buffer upon the magnification in the axial direction is taken into account by multiplying the one retrieved from the fit Z-coordinate by 0.79 (Egner and Hell, 2006), (Huang, et al., 2008) in case of mounting in an aqueous solution.

The FRC curve is calculated similarly to a previously described method (Nieuwenhuizen *et al*., 2013). First, the input eventlist is shuffled randomly using the Matlab function 'randperm'. The shuffled list is divided into two consecutive parts, approximately equal in length. From each, a histogram-mode image with sampling of 10 nm is built. A 2D Tukey window is applied to each image in the form of w2 = w * w`, where w = tukeywin (L, r), L is the size of the images in pixels (here L = 1800), r is a proportion of L that is equal to a part of a cosine function (here r = 0.25). The images are transformed into Fourier space by 'fftshift', and are divided into n rings with widths $w_{ri} = r_i - r_{i-1} = L/n$. For each ring, the FRC-value is calculated by the formula

$$FRC(q) = \frac{\sum_{\vec{q} \in circle} f_1(\vec{q})\, f_2(\vec{q})^*}{\sqrt{\sum_{\vec{q} \in circle} |\, f_1(\vec{q})|^2}\, \sqrt{\sum_{\vec{q} \in circle} |\, f_2(\vec{q})|^2}}$$

where $f_1(\vec{q})$ and $f_2(\vec{q})$ are the Fourier transforms of the two images. To get the resolution at 1/7 of FRC, the FRC-curve is smoothed by 'loess' (local regression using weighted linear least squares and a 2nd degree polynomial model) algorithm (Cleveland, 1979), and the first intersection of the smoothed curve with the value FRC = 1/7 is taken as the nominal resolution value.

Super-resolution imaging

HeLa cells were plated in a 4-compartment glass-bottom petri dish (CELLView, Greiner Bio-One) and fixed with 4% formaldehyde for 20 min in phosphate-buffered saline (PBS). After permeabilization with 0.1% Triton in PBS (PBS/Tx) twice for 10 min, the primary antibody (anti-β-tubulin monoclonal 1Tub-2A2, in house IGBMC) at 500x dilution in PBS/Tx was incubated overnight at 4 °C. The sample was then washed with PBS/Tx three times over 2 hours, and the secondary antibody (Goat anti-mouse Alexa Fluor-647 conjugated, Invitrogen) in dilution 4 µg/ml in PBS/Tx was incubated for 2 hours at room temperature. Subsequently, the cells were washed in PBS/Tx three times for 2 hours, then briefly three times in PBS. Prior to imaging, the sample was mounted in a PBS buffer that contained 10 mM of cysteamine and 25 mM of HEPES (pH 7.5).

The super-resolution experiments were performed on a Leica SR GSD system built on a base of DMI6000 B inverted wide-field microscope. We used the HCX PL APO 100x/1.47 Oil CORR TIRF PIFOC objective with 1.6x magnification lens that provides an equivalent pixel size of 100 nm on Andor iXon3 DU-897U-CS0-#BV EMCCD camera with a field of view of 18x18 µm in GSDIM mode. Continuous wave fiber lasers (MPBC Inc., 488 nm 300 mW, 532 nm 1000 mW, 642 nm 500 mW) and a diode laser (405 nm 30 mW) were utilized for excitation. The microscope is also equipped with the suppressed motion (SuMo) sample stage, which can reduce drift only to some extent, i.e. it cannot eliminate it (typical values 20-50 nm over 10 min).

The β-tubulin-labelled sample was first illuminated with the 100% laser power to quickly send the fluorophores into the dark state. The acquisition was started automatically after beginning of observation of single-fluorophore events ("blinking") that corresponded to the drop of the frame correlation value to 0.2 in the corresponding wizard in the LAS AF software. After a few minutes, as the number of blinking evens dropped, the sample started to be illuminated additionally by a 405 nm laser with gradual increase of its intensity in order to keep a nearly constant rate of single-molecular returns into the ground state. The acquisition was stopped after almost complete bleaching of the fluorophore.

For the multi-color imaging, the Tetraspeck multi-color beads were imaged sequentially: first by excitation with the 642-nm laser at 5% of its maximum power, then with the 488 nm one at 32% of power. The exposure time of a frame was 30 ms, the EM gain of the camera was 300 times.

The localization and fitting of single-molecule events were performed in real time during acquisitions in Leica LAS AF 3.2.0.9652 software with the "center of mass" fitting method. The

drift was detected using a pixel size of 20 nm, 10-11 consecutive sublists and histogram representation of sub-images for cross-correlation detection. For testing purposes, circular drift was added using the formula $x_i = x_{0i} + R \cdot \cos(2\pi n_i)$, $y_i = y_{0i} + R \cdot \sin(2\pi n_i)$, where x_{0i}, y_{0i} are the coordinates of an event i in the original dataset, R is the radius of the circle, $n_i = i/N$, N is the total number of events; R was set to 25 nm. In this case, the value of the angular shift is proportional to the number of the event; the drift circumscribes the full circle on the full duration of the acquisition.

The FRC curves were calculated in 90 concentric rings using histogram representation of half-datasets, unless stated differently. Prior to calculation the FRC, the eventlists were sieved by merging of repetitive localizations within a radius of 50 nm because these events may influence the FRC curve yielding too optimistic values (Banterle *et al*., 2013). For statistics, the FRC curves and the resolution values were calculated 50 times for each localization table. The FRC curves for histogram, Gaussian and Voronoi representations were also calculated by the FSC program (Image Science Software GmbH) (van Heel *et al*., 1996) confirming the results obtained with SharpViSu.

References

Andronov,L. *et al.* (2016) ClusterViSu, a method for clustering of protein complexes by Voronoi tessellation in super-resolution microscopy. *Sci. Rep.*, in press.

Abbe,E. (1873) Beiträge zur Theorie des Mikroskops und der mikroskopischen Wahrnehmung. *Arch. Mikrosk. Anat.*, **9**, 413–468.

Baddeley,D. *et al.* (2010) Visualization of Localization Microscopy Data. *Microsc. Microanal.*, **16**, 64–72.

Banterle,N. *et al*. (2013) Fourier ring correlation as a resolution criterion for super-resolution microscopy. *J. Struct. Biol.*, **183**, 363–367.

Born,M. and Wolf,E. (1999) Principles of Optics: Electromagnetic Theory of Propagation, Interference and Diffraction of Light. Cambridge University Press, Cambridge, 461–475.

Cleveland,W.S. (1979) Robust Locally Weighted Regression and Smoothing Scatterplots. *J. Am. Stat. Assoc.*, **74**, 829–836.

Delaunay,B. (1934) Sur la sphère vide. A la mémoire de Georges Voronoï. *B. Acad. Sci. URSS*, **6**, 793–800.

Deschout,H. *et al.* (2014) Precisely and accurately localizing single emitters in fluorescence microscopy. *Nat. Methods* **11**, 253–266.

Edelstein,A.D. *et al*. (2014) Advanced methods of microscope control using μManager software. *J. Biol. Methods*, **1**, e10.

Egner,A. and Hell,S.W. (2006) Aberrations in confocal and multi-photon fluorescence microscopy induced by refractive index mismatch. In Pawley,J. (ed.) *Handbook of Biological Confocal Microscopy*, 3rd edn. University of Wisconsin, Madison, pp. 404–413.

Endesfelder,U. and Heilemann,M. (2014) Art and artifacts in single-molecule localization microscopy: beyond attractive images. *Nat. Methods* **11**, 235–238.

El Beheiry,M. and Dahan,M. (2013) ViSP: representing single-particle localizations in three dimensions. *Nat. Methods*, **10**, 689–690.

Guizar-Sicairos, M., Thurman, S. T. & Fienup, J. R., 2008. Efficient subpixel image registration algorithms. *Opt. Lett.* **33**, 156–158.

Henriques,R. *et al*. (2010) QuickPALM: 3D real-time photoactivation nanoscopy image processing in ImageJ. *Nat. Methods*, **7**, 339–340.

Huang,B. *et al.* (2008) Three-dimensional super-resolution imaging by stochastic optical reconstruction microscopy. *Science,* **319**, 810–813.

Juette,M.F. *et al.* (2008) Three-dimensional sub–100 nm resolution fluorescence microscopy of thick samples. Nat. Methods **5**, 527–529.

Nieuwenhuizen,R.P.J. *et al*. (2013) Measuring image resolution in optical nanoscopy. *Nat. Methods,* **10**, 557–562.

Ober,R.J. *et al.* (2004) Localization Accuracy in Single-Molecule Microscopy. *Biophys. J.* **86,** 1185–1200.

Ovesný,M. *et al.* (2014) ThunderSTORM: A Comprehensive ImageJ Plug-in for PALM and STORM Data Analysis and Super-Resolution Imaging. *Bioinformatics* **30**, 2389–90.

Pavani, S. R. P. *et al.* (2009) Three-dimensional, single-molecule fluorescence imaging beyond the diffraction limit by using a double-helix point spread function. *Proc. Natl. Acad. Sci. USA* **106,** 2995–2999.

Pengo,T. *et al.* (2015) PALMsiever: a tool to turn raw data into results for single-molecule localization microscopy. *Bioinformatics*, **31**, 797–798.

Rees,E.J. *et al.* (2013) Elements of image processing in localization microscopy. *J. Opt.*, **15**, 094012.

Rieger,B. and Stallinga,S. (2014). The Lateral and Axial Localization Uncertainty in Super-Resolution Light Microscopy. *ChemPhysChem* **15**, 664–670.

Sibson,R. (1981) A Brief Description of Natural Neighbour Interpolation. In Barnet V. (ed.) *Interpreting Multivariate Data*, Wiley, Chichester, pp. 21–36.

Smith,A.R. (1978) Color gamut transform pairs. *Comp. Graph.,* **12**, 12–19.

Szymborska,A. *et al*. (2013) Nuclear pore scaffold structure analyzed by super-resolution microscopy and particle averaging. *Science,* **341**, 655–658.

van Heel,M. *et al*. (1996) A new generation of the IMAGIC image processing system. *J. Struct. Biol.,* **116**, 17–24.

Voronoi,G. (1908) Nouvelles applications des paramètres continus à la théorie des formes quadratiques. *J. Reine Angew. Math.,* **133**, 97–178.

Wolter,S. *et al*. (2012) rapidSTORM: accurate, fast open-source software for localization microscopy. *Nat. Methods*, **9**, 1040–1041.